

Room Temperature Optically and Magnetically Active Edges in Phosphorene Nanoribbons

¹Arjun Ashoka, ^{2,3}Adam J. Clancy[#], ⁴Naitik A. Panjwani[#], ¹Nicholas J. M. Popiel, ¹Alex Eaton, ⁵Thomas G. Parton, ⁶Loren Picco, ¹Sascha Feldmann, ³Rebecca R. C. Shutt, ¹Remington Carey, ³Eva S. Y. Aw, ^{2,7,8}Thomas J. Macdonald, ⁹Marion E. Severijnen, ⁹Sandra Kleuskens, ¹⁰Hilton Barbosa de Aguiar, ¹Richard H. Friend, ⁴Jan Behrends, ⁹Peter C.M. Christianen, ³Christopher A. Howard, ¹Akshay Rao and ^{1,10}Raj Pandya ✉

¹Cavendish Laboratory, University of Cambridge, J.J. Thomson Avenue, CB3 0HE, Cambridge, United Kingdom

²Department of Chemistry, UCL, Christopher Ingold Building, Gordon St, London WC1H 0AJ, UK

³Department of Physics & Astronomy, University College London, London, WC1E 6BT, United Kingdom

⁴Berlin Joint EPR Lab, Fachbereich Physik, Freie Universität Berlin, D-14195 Berlin, Germany

⁵Yusuf Hamied Department of Chemistry, University of Cambridge, Lensfield Road, Cambridge, CB2 1EW, United Kingdom

⁶Department of Physics, Virginia Commonwealth University, Richmond, VA, USA

⁷Department of Chemistry and Centre for Processable Electronics, Imperial College London, London, W12 0BZ, United Kingdom

⁸School of Engineering and Materials Science, Queen Mary University of London, London E1 4NS, United Kingdom

⁹High Field Magnet Laboratory (HFML - EMFL), Radboud University, 6525 ED, Nijmegen, The Netherlands

¹⁰Laboratoire Kastler Brossel, ENS-Université PSL, CNRS, Sorbonne Université, Collège de France, 24 rue Lhomond, 75005, Paris, France

[#]Denotes equal contribution

Correspondence: rp558@cam.ac.uk

Nanoribbons – nanometer wide strips of a two-dimensional material – are a unique system in condensed matter physics. They combine the exotic electronic structures of low-dimensional materials with an enhanced number of exposed edges, where phenomena including ultralong spin coherence times¹⁻⁴, quantum confinement⁵ and topologically protected states⁶⁻⁸ can emerge. An exciting prospect for this new material concept is the potential for both a tunable semiconducting electronic structure and magnetism along the nanoribbon edge. This combination of magnetism and semiconducting properties is the first step in unlocking spin-based electronics such as non-volatile transistors, a route to low-energy computing⁹, and has thus far typically only been observed in doped semiconductor systems and/or at low temperatures¹⁰⁻¹⁵. Here, we report the magnetic and semiconducting properties of phosphorene nanoribbons (PNRs). Static (SQUID) and dynamic (EPR) magnetization probes demonstrate that at room temperature, films of PNRs exhibit macroscopic magnetic properties, arising from their edge, with internal fields of ~ 250 to 800 mT. In solution, a giant magnetic anisotropy enables the alignment of PNRs at modest sub-1T fields. By leveraging this alignment effect, we discover that upon photoexcitation, energy is rapidly funneled to a dark-exciton state that is localized to the magnetic edge and coupled to a symmetry-forbidden edge phonon mode. Our results establish PNRs as a unique candidate system for studying the interplay of magnetism and semiconducting ground states at room temperature and provide a stepping-stone towards using low-dimensional nanomaterials in quantum electronics.

Over the last 40 years, strategies to couple different magnetic phenomena and the electronic ground states of semiconductors have mostly focussed on doping traditional semiconductors with certain transition metals to form so-called dilute magnetic semiconductors (DMSs)^{16–20}. A more recent approach has been to exploit the unique spin configurations that can be realised in two-dimensional (2D) monolayer materials – some of which, such as CrSBr and NiPS₃, have been also shown to host (at low temperature) semiconducting magnetic phases^{21–24}. Slicing two-dimensional monolayers into thin strips – nanoribbons – opens the possibility for an even wider range of magnetic spin-arrangements across and along the ribbon edges, whilst retaining the favourable electronic and mechanical properties of 2D systems. The most intensely studied nanoribbons thus far have been those based on the flat, honeycomb lattice of graphene^{25,26}, where at low temperatures topologically-engineered bands^{6,7,27} and a range of spin ordered electronic states have been observed^{1,8}. However, the laborious chemical synthesis^{28,29} combined with challenging edge-functionalisation^{1,8} – akin to magnetic doping in DMSs – necessary to achieve the aforementioned phenomena, represents a significant challenge for both practical use and exploring novel physics in GNRs. These problems are further compounded by the short length (sub-100 nm) that GNRs can be limited to and the fact that spintronic properties often emerge only at low-temperatures. Consequently, there is a need to explore nanoribbon systems which can be produced at scale and exhibit room-temperature intrinsic spintronic and electronic properties. Among the mooted systems, phosphorene nanoribbons (PNRs) – the black phosphorus analogue to GNRs – have uniquely been proposed. Although PNRs are expected to host many superlative characteristics, the predicted presence of excitonic effects and room temperature ferromagnetism^{2,30–33} makes them particularly intriguing. The highly anisotropic crystal and electronic structure of PNRs opens the possibility for a wide range of spin interactions both in- and out-of-the plane, with their visible band-gap making them well-suited for studying and utilising the interplay between functional optoelectronic properties and magnetism in low-dimensions^{9,34}.

In this work, we focus on PNRs that are produced readily in batch solutions with typical ribbon widths of ~10 nm and lengths up to 1 μm (see methods)^{35,36}. The long edges of the PNRs are exclusively zigzag terminated³⁵. **Figure 1a** shows an AFM image of a representative monolayer ribbon (height 0.48 ± 0.14 nm and width 8.12 ± 1.08 nm) along with histograms of the width and height distribution along the ribbon measured using high speed AFM. The green arrow indicates the long direction of the ribbon with zigzag terminated edges. Quantum Monte Carlo and dynamic mean field theory calculations have predicted that such zigzag PNRs host room temperature ferromagnetism on their edges with an energetic difference of just 1 μeV per spin between the edge-to-edge ferromagnetic (FM) and antiferromagnetic (AF) spin aligned ground state^{33,37,38}. Furthermore, these edge magnetic states are expected to be robust to external disorder and strain and the widths that we study are in the crossover regime between the decoherence-dominated classical magnetism and fluctuation-dominated quantum magnetism studied in graphene nanoribbons^{37,39,40}.

To investigate the magnetic ground state of PNRs, it is important to first establish the degree of intrinsic magnetic anisotropy^{41,42}, due to their highly anisotropic shape and crystal structure. A non-invasive route to accessing the magnetic anisotropy of nanoobjects dispersed in solution is to measure the magnetic field-induced alignment through the linear dichroism (LD) and linear birefringence (LB)⁴³. The principle behind optically-detected magnetic alignment is that a magnetically-anisotropic nano-object orients in a magnetic field to minimise its magnetic orientational energy, which can eventually overcome thermal fluctuations. The optical anisotropy (LD or LB) of the underlying nanoobject can then serve as a sensitive probe of the degree of alignment due to the external magnetic field. As shown in **Figure 1b**, we observe

very unexpected behaviour in the magnetic linear birefringence, with the orientational anisotropy saturating at near 10 T at room temperature, much lower than that of other known

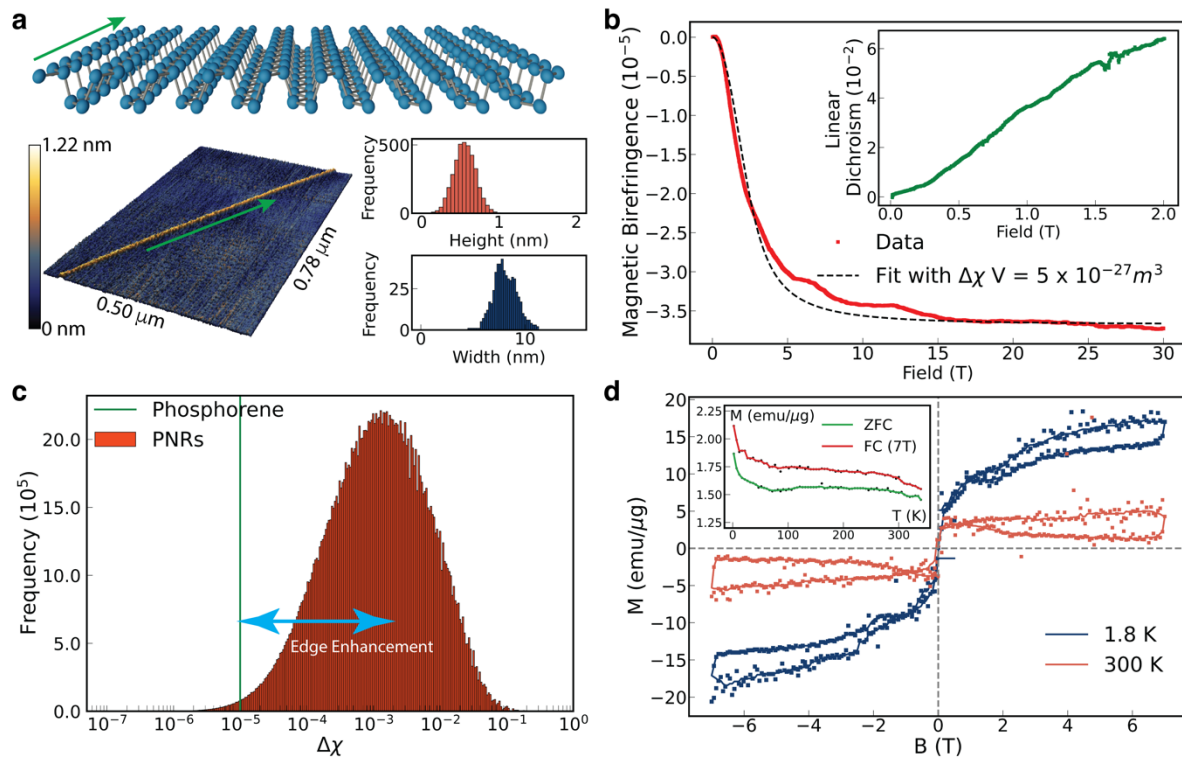


Figure 1: Shape, magnetic and optical anisotropy of PNRs: **a.** (Top) Crystal structure of the synthesised PNRs with the zigzag edges along their long axis (green arrow). (Bottom) Representative AFM image and histogram of height and width along a single ribbon. An average width of 8 nm and average monolayer height of 0.6 nm is found along the ribbon. **b.** Alignment of PNRs in solution measured using magnetic field induced linear birefringence up to 30 T shows a saturation at 10 T. Combined with the magnetic linear dichroism (inset), these result suggest that PNRs align with their short axis along the field direction. **c.** Calculated histogram of the intrinsic anisotropy in the magnetic susceptibility shows a 100-fold edge enhancement from the previously reported monolayer phosphorene limit. **d.** Isothermal magnetisation of PNR at 1.8 K (blue) and 300 K (red) measured using a SQUID magnetometry. Ferromagnetic-like correlations up to room temperature are demonstrated by the hysteresis. The inset displays the field-cooled (FC) at 7 T and zero-field cooled (ZFC) magnetisation as a function of temperature for the same PNR samples.

nanomaterials^{44–46}. On fitting the data to the orientational magnetic energy (see **Supplementary Note 1**), we retrieve the anisotropy in the volume magnetic susceptibility ($\Delta\chi$) multiplied by the volume of the material, $\Delta\chi V = 5 \times 10^{-27} \text{ m}^3$. We additionally observe a magnetic field induced LD signal at 543 nm, with more light absorbed when the light is polarised along the magnetic field direction (**Figure 1b**, inset). PNRs are expected to have a higher absorption cross section with light polarised perpendicular to the zigzag direction, as has been reported experimentally for phosphorene and obtained from GW-BSE calculation on PNRs^{31,42}. We hence conclude that in a magnetic field, the ribbons orient with their short axis along the field direction.

We then use reported histogram distributions of the length, width and height of 940 PNRs, measured using TEM to calculate the approximate distribution of ribbon volumes in the solution³⁵. From this and the calculated $\Delta\chi V$, we extract the anisotropy in the dimensionless magnetic susceptibility $\Delta\chi \approx 10^{-3}$ (**Figure 1c**). This is two orders of magnitude larger than the value expected for a single layer of phosphorene, using extrapolated values from reports of

$\Delta\chi$ for layered phosphorene, *i.e.*, black phosphorous (**Figure 1c**, green line) . The latter has its predominant magnetic anisotropy between the in- and out-of-plane directions, which are not expected to be the dominant anisotropy directions here⁴¹. We infer that this 100-fold enhancement in the $\Delta\chi$ must therefore arise from the enhanced number of edges of the ribbons as this is the only intrinsic difference between phosphorene and the PNRs. The origin of the large $\Delta\chi$ could be from diamagnetic, paramagnetic or ferromagnetic anisotropies, or a combination of these. It is therefore critical to establish the presence of unpaired spins in the PNR system, which would point to a para- or ferromagnetic origin for the large $\Delta\chi$, and the presence of the predicted edge magnetism.

In order to do this, we performed SQUID magnetometry on a deposited ensemble of drop-cast PNRs in the solid state⁴⁷. The 7 T-field cooled (FC) and zero field cooled (ZFC) magnetisation measured in a 50 mT field (**Figure 1d**, inset) shows non-Curie behaviour as we approach temperatures as high as 350 K where the two curves approach each other but do not yet overlap. We performed isothermal magnetic field sweeps at 1.8 and 300 K to study the hysteretic nature of the spin couplings (**Figure 1d**). We observe an atypical ferromagnetic-like hysteresis at both 300 K and 1.8 K with a coercive field of near 50 mT with the hysteretic behaviour disappearing at small applied fields. This is consistent with the prediction of two competing AF and FM ground states in the system³⁷. Upon applying a small external field of the order of 50 mT, the ferromagnetic interaction energy is lowered by ~ 1 μeV per spin (using 1 Bohr magneton and $\Delta E = -\mu \cdot B$, for the unpaired electrons in PNRs³⁸). Hence the degeneracy of the FM and AFM ground state is lifted, and away from zero-field, the FM phase forms the ground state associated with the hysteretic behaviour. This does not change when measured in lower projecting fields of 20 mT (**Supplementary Note 2**), indicating that the behaviour does not emerge due to an interaction with the measurement/projecting field of the SQUID. In the solution phase (NMP and DMF solvents), we also find that the FC and ZFC magnetisations are split up to the freezing point of the solvent (**Supplementary Note 2**), above which the liquid dispersions are no longer macroscopic magnetic systems. We repeat the solution measurements on oxygenated PNRs by bubbling air through the solution to chemically terminate the ribbon edge (hydrogenated, phosphate, carboxylate, *etc*, based terminuses^{35,48–50}) and find a purely diamagnetic response (**Supplementary Note 2**)^{51,52}. Elemental analysis (inductively coupled plasma optical emission spectroscopy (ICP-OES)) of the same PNR solutions estimates less than 20 parts per billion of Fe, Co, Ni, Cr and Mn, ruling these out as

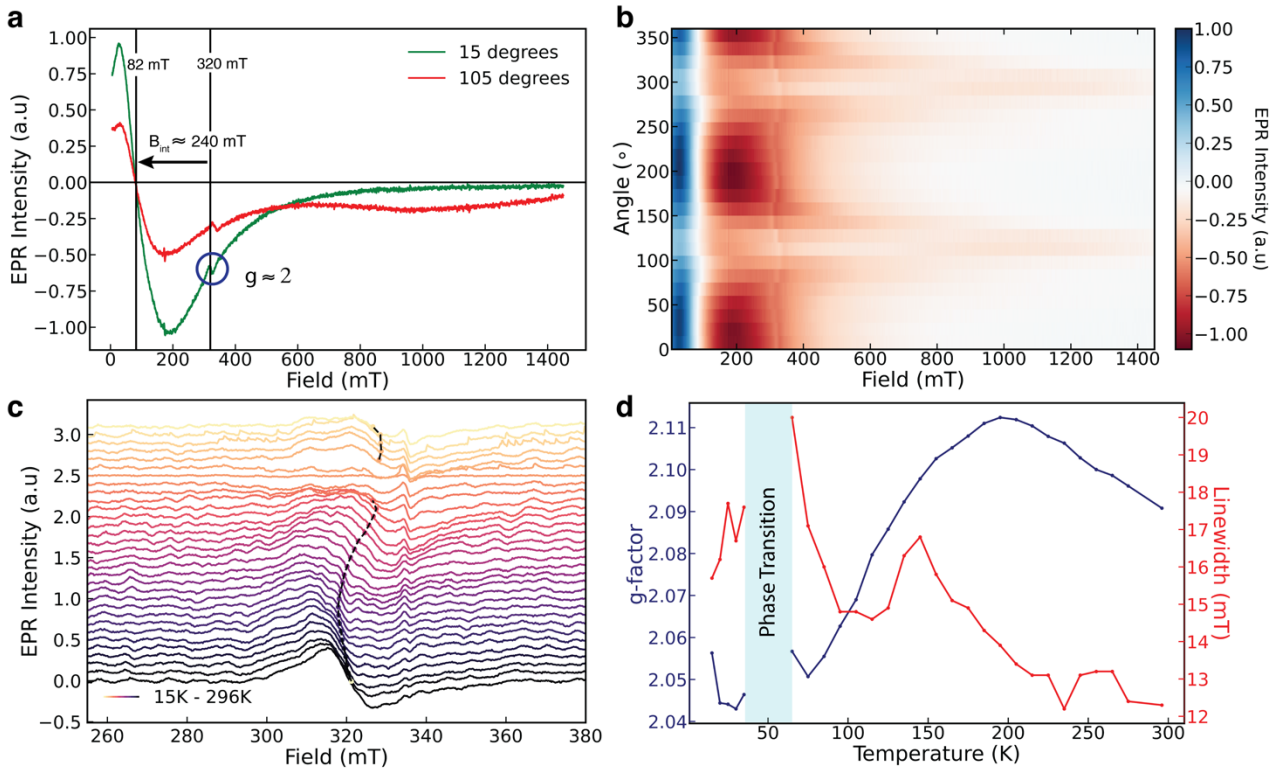


Figure 2: EPR and FMR-like local magnetic correlations: **a.** cwEPR signal of PNRs in the solid state measured over a wide magnetic field range shows both the unpaired electron peak at 320 mT sitting atop of a much larger ferromagnetic-like resonance at 82 mT, suggesting an internal field of 240 mT (green curve; 15 degrees – low field signal: internal field aligned to magnetic field). The sample is highly inhomogeneous hence rotation results in a shift in the resonance positions (red curve; 105 degrees – high field signal: internal field anti-aligned to magnetic field). **b.** Orientational magnetic anisotropy in EPR signal across full range of angles. **c.** Line cuts of $g \approx 2$ signal along with the zero-intensity lines (dashed black) **d.** Extracted g -factor and linewidth as a function of temperature. We observe a divergence in the linewidth around 70 K characteristic of a phase transition.

the signal origin (**Supplementary Note 3**). Overall, this suggests that the magnetic response of PNRs arises, as predicted in numerous studies, from the ribbon edge with the persistence of the magnetic behaviour up to room temperature^{33,37,38}.

Next, we investigate the local spin correlations along the edge of the PNR by performing continuous wave electron paramagnetic resonance (cwEPR) measurements on a film formed on the inner wall of an EPR sample tube. Consistent with hypothesis of unpaired electrons at the ribbon edge we observe, in **Figure 2a,c**, a broad ≈ 12 -19 mT wide $g \approx 2$ EPR signal at room temperature. To our surprise, a wider magnetic field scan (0-1400 mT) reveals much more intense and even broader FMR like signals (**Figure 2a**). The EPR and FMR signals both show a strong orientation dependency when rotating around the sample tube long axis as shown in **Figure 2b**. This behavior arises from the inhomogeneity of the inner wall film in thickness, packing, PNR orientations and size.

The FMR signals seen in **Figure 2a,b** and the observed orientation behavior is complex due to the inhomogeneity occurring from the inner wall sample. However, in order to shed some light on the internal fields within the sample, we fit the experimental data with two purely Lorentzian and one Voigtian component (see **Supplementary Note 4**). We find that some PNR domains give rise to net internal fields of ≈ 225 -265 mT and are aligned to the external magnetic field direction, thereby shifting the effective resonance position to lower magnetic fields, at around ≈ 55 -95 mT. These PNR domains show very little change in effective resonance positions with changing orientation suggesting they are easily (re-)magnetised. We also see certain PNR domains where the effective resonance position is strongly orientation dependent, ranging from

850 mT to 240 mT. The significant change in the resonance position with changing orientation suggests these domains are hard to (re-)magnetize, resulting in low field signals when the net internal field is (close to) aligned to the external magnetic field direction and high field signals when the net internal field is anti-aligned to the external magnetic field direction. We estimate the net internal field magnitude of these PNR domains to be ≈ 600 mT considering the minimum and maximum resonance positions achieved *via* sample rotation. PNR domains exhibiting an easy and hard axis could explain the FMR like signals with weak and strong orientating dependency respectively. The broad linewidths of all FMR like signals suggests a wide distribution of internal fields within each domain. This FMR behaviour is strongly reminiscent of reports of magnetism in Ni nanocubes where the different size nanocubes exhibit different internal fields and distributions of internal fields, leading to this rich orientation dependent behaviour⁵³ (see **Supplementary Note 4** for further discussion).

Focusing again on the $g \approx 2$ EPR signal, we see that the g -factor and linewidth vary as a function of sample tube rotation, with the g -factor ranging from 2.03 to 2.21 (see **Supplementary Note 4**). The g -factor for black phosphorous has been calculated to be 2.0 in-plane and 2.14 out-of-plane in the monolayer (1L) limit, with a strong layer number dependence, reaching 2.9 in the bulk out-of-plane limit⁵⁴. The calculated out-of-plane g -factor for a 2 layer (2L) black phosphorous is ≈ 2.21 . Hence the observed EPR signal, results predominantly from 1L and 2L PNRs, consistent with Watts *et al.*³⁵, and the spin polarisation is either in-plane or out-of-plane depending on the tube orientation.

The EPR signal also shows a strong temperature dependency, where the linewidth and g -factor behaviour are non-monotonic, with the divergence of the linewidth and the disappearance of the signal around 55 K, which reappears at lower temperatures. This behaviour which also appears, albeit weakly, in the SQUID magnetisation (**Figure 1d**, inset), is characteristic of a phase transition, however further work is required to describe its nature. We note that the Raman spectrum shows no significant evolution with temperature (300 K to 10 K) that would be indicative of a structural phase transition (**Supplementary Note 5**). We suggest that the smooth temperature dependence of the g -factor from 300 to 75 K could signal a slow spin-canting in the out-of-plane direction due to AF correlations which lowers the g -factor from the fully out-of-plane polarised value of 2.14 towards the in-plane value of 2.00⁵⁵.

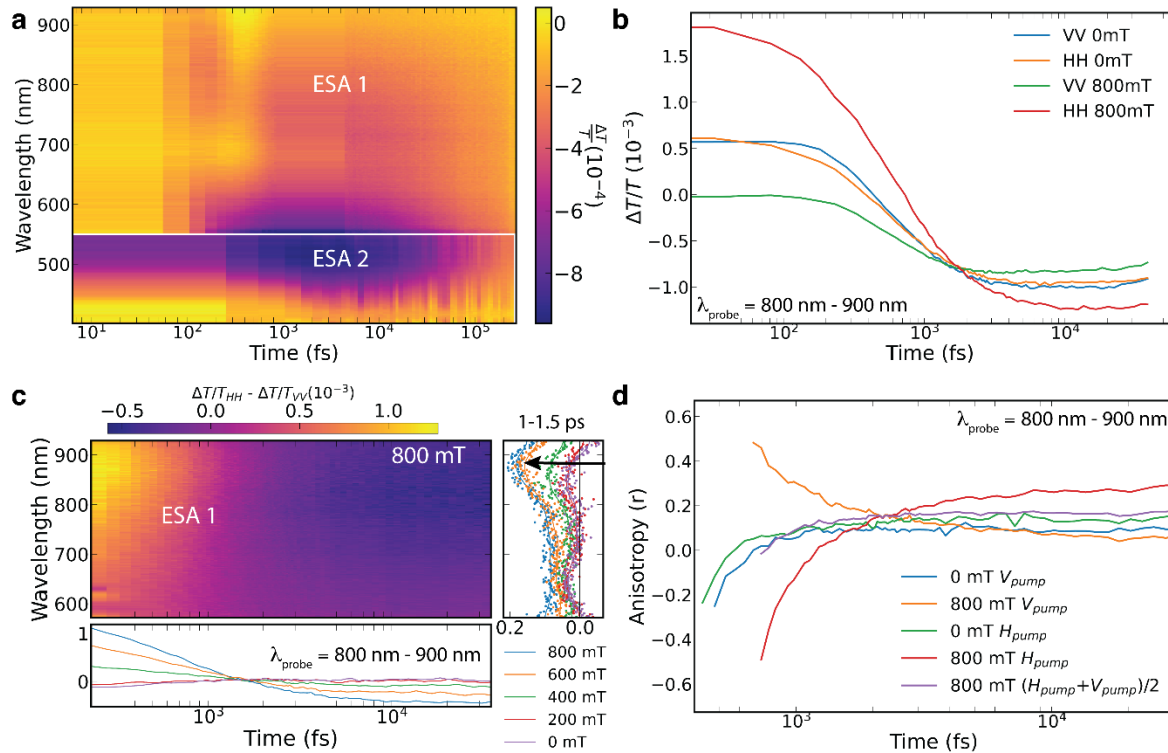


Figure 3: Photoexcited dipole relaxation dynamics. **a.** Broadband transient absorption spectrum of PNRs. Upon photoexcitation the PNRs display two broad excited state absorption (ESA) bands that decay on the order of ns. There appears to be a broad photobleaching spectra signature at 700 nm that overlaps with the ESA bands. **b.** Polarisation and magnetic field resolved decay of ESA 1 kinetics. Upon application of a 800 mT field, the ribbons align in the magnetic field, splitting the degeneracy of the HH and VV polarised experiments. Further, we find a significant reduction in the signal magnitude when photoexciting V polarised (along the PNR long axis). **c.** Magnetic field induced anisotropy obtained by subtracting the spectral response of the unaligned ribbons. This unveils a spectral signature centred at 850 nm (corresponding to ESA 1), the magnitude of which can be strongly modulated with a sub-1T field (right panel). **d.** Decay of polarisation anisotropy (r) as a function of magnetic field. In an unpolarised solution under no magnetic field, we find that the anisotropy is initially -0.2 and decays to close to 0 within 1 ps (green and blue), indicating the photoexcited state is perpendicular to the probed state after 1 ps (the differences in the V and H polarised experiments at 0 mT demonstrate the setup's resolution). Upon application of the 800 mT field however, photoexciting V polarised (PNR long axis, orange curve) we find that the anisotropy retains its' sign (indicating the photoexcited state is the same orientation as the probed one) whereas when photoexciting H polarised (PNR short axis, red curve), the anisotropy flips sign, indicating a dipole flip, as in the unpolarised case, with the average converging to the unpolarised system, as expected.

Having established the signatures of key spin correlations and room temperature magnetism in PNRs, we turn to their optical properties. The temperature dependent absorption spectrum of PNRs is broad and featureless (see **Supplementary Note 6**), we hence interrogate the optical properties by studying the photophysical dynamics³⁵. Upon photoexcitation with a 460 nm, 250- fs pulse, we see the emergence of two long lived (nanosecond) excited state absorptive (ESA) bands at 800 nm (ESA 1) and 500 nm (ESA 2) along with an overlapping, short-lived (picosecond) broad photobleaching band at 700 nm (**Figure 3a**).

From the LD in a magnetic field (**Figure 1b**, inset), we know that the ribbons align with their short axis along the magnetic field direction in solution. In **Figure 3b**, we show the results of performing polarization resolved pump-probe experiment on the PNRs in solution, with an 800 mT applied external magnetic field in the Faraday geometry. We find that the typical co-polarised horizontal (HH) and vertical pump and probe (VV) signal's degeneracy is lifted and a lab axis is introduced into the experiment upon application of an 800 mT field. The magnetic

field is polarised along the H direction in the lab axis which, as expected, results in the higher transient absorption signal due to the increased net linear dichroism along the HH direction (**Figure 1b**). Further, as expected, we see the alignment effect scales with the applied field strength (**Supplementary Note 7**).

We leverage this magnetic alignment effect to isolate the spectral features of the magnetically aligned ribbons (as opposed to optical signatures of a non-magnetic sub-population) by subtracting the HH and VV polarised transient absorption maps at different field strengths, as any unaligned ribbons would have identical HH and VV polarised transient absorption maps yielding no difference signal. As seen in **Figure 3c**, we find that the magnitude and kinetics of the photoinduced absorption band (ESA 1) is most strongly perturbed by the external field. We can therefore confidently assign ESA 1 to that of the magnetically active ribbons.

Having established a spectral signature of the magnetically active ribbons, we use this feature to track the evolution of the photoexcitation in time in the magnetically active ribbons through the transient absorption anisotropy in the ESA 1 band (800-900 nm) defined as,

$$r = \frac{\frac{\Delta T}{T_{\parallel}} - \frac{\Delta T}{T_{\perp}}}{\frac{\Delta T}{T_{\parallel}} + 2 \frac{\Delta T}{T_{\perp}}},$$

where $\frac{\Delta T}{T_{\parallel}}$ and $\frac{\Delta T}{T_{\perp}}$ are the transient absorption signal with the probe polarisation parallel and perpendicular to the pump polarisation⁵⁶. We find that at 200 fs the anisotropy is -0.2, signifying that we are likely probing the dipole polarised orthogonally to the main photoexcited transition. Over 1 ps, the anisotropy relaxes to a value of about 0.05, signifying that there is energetic transfer between the dipoles as the timescale is faster than the ns-orientational relaxation dynamics typically associated with molecular anisotropy. As expected, we demonstrate the H and V pumped anisotropies are degenerate, demonstrating the instrument resolution (**Figure 3d**, blue and green).

Upon application of the 800 mT field due to the macroscopic alignment of the ribbons, we are able to increase our dipole selectively and pump the short-axis polarised (H) and long-axis polarised (V) dipole. It is worth noting that as the ribbons are now aligned, the sign of the anisotropy is the key feature of interest, as the value of the anisotropy will not be consistent with the isotropic molecular distribution assumption standard to such measurements⁵⁷. We find that when pumping the long-axis polarised (V) dipole (**Figure 3d**, orange), the anisotropy does not change sign, indicating that the energy remains in this state, whereas when we pump the short-axis polarised (H) dipole, the sign flips (red), just like in the case of the unpolarised ribbons (blue). Further, the fact that we can construct the unaligned PNR anisotropy as an average of pumping the 800 mT aligned long-axis polarised (V) and short-axis polarised (H) dipoles (**Figure 3d**, purple) confirms that these are the main two dipoles involved in the optical response of the system. Taken together with the larger magnitude of the transient absorption signal (**Figure 3b**) of the H pumped system, this suggests that the photoexcitation is initially predominantly polarised along the short axis and transfers to an orthogonal dipole polarised along the PNRs long axis on a sub-1ps timescale.

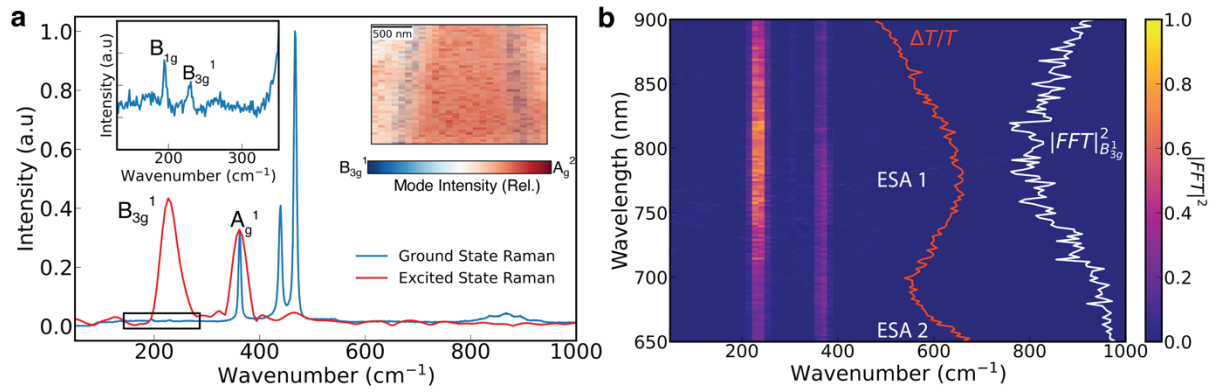


Figure 4: Coupling of the photoexcitation to the magnetic edges **a.** Excited state (impulsive, time domain) Raman spectrum of the PNRs (red) shows a strong coupling to the B_{3g}^1 mode compared to the ground state spectrum (blue), indicating that the photoexcitation is delocalised along the edges of the ribbon. Inset: (Left) Zoom into low frequency region of ground state Raman spectrum. (Right) Raman imaging of a black phosphorous flake shows that, as previously reported⁵⁸, the B_{3g}^1 mode is localised on the edge. **b.** Wavelength resolved, impulsive, time-domain Raman spectrum of the photoexcited PNRs reveals that the B_{3g}^1 mode is most strongly coupled (white curve) to ESA 1 (red curve) which was also most strongly modulated by the external magnetic field.

GW-BSE calculations of the optical spectrum of zigzag PNRs report that the lowest excited state is a dark exciton which is polarised along the ribbons long axis³¹. We propose that the primary photoexcitation mechanism is therefore that the initial excitation dipole polarised along the ribbon short axis decays to this long axis polarised dark exciton on sub-1ps timescales. This is consistent with the fast disappearance of the photo bleach signal corresponding to the initial state in the transient absorption (**Figure 3a**) with the formation of long lived ESAs likely from the dark exciton.

While calculations have reported that the first bright exciton in zigzag PNRs has significant density along the ribbon edges, it is unclear whether this lower energy dark exciton that the photoexcitation decays to is also localised along the ribbon edges³¹. This is critical for any potential excited state magneto-optical coupling in PNRs, as most of the photoexcitation lifetime appears to be spent in this state. We exploit the presence of special localised phonon modes on the edges of black phosphorous to study this⁵⁸.

The spontaneous Raman spectrum of the PNRs (**Figure 4a**, blue curve) is dominated by the A_g^1 , B_g^2 and A_g^2 modes, all of which are also observed in bulk black phosphorous (BP)⁵⁹. We demonstrate the previously-reported, bulk-symmetry forbidden B_g^1 and B_{3g}^1 edge phonon modes along the zigzag edge of BP using Raman imaging (**Figure 4a**, inset)⁵⁸. In order to study the mode coupling to the excited state energy surface, we perform impulsive vibrational spectroscopy (IVS) using broadband compressed 13-fs pulses centred at 550 nm. We find that when resonantly photoexciting the PNRs, the photoexcited state is strongly coupled to the B_{3g}^1 edge phonon mode (**Figure 4a**, red curve). Control experiments with off-resonant IVS on the PNRs and DMF solvent confirm that the B_{3g}^1 edge phonon mode is indeed dominantly coupled to the excited state potential energy surface (see **Supplementary Note 8**). Furthermore, as seen in **Figure 4b**, we find that this edge phonon mode is most strongly coupled to ESA 1, the transition characteristic of the magnetically active ribbons. The mode selectivity of the excited state coupling to edge mode as compared to the bulk modes suggests that the electron density of the photoexcitation is along the edges of the PNRs. In the solution phase, we observe that the excited state IVS of the B_{3g}^1 out-of-plane edge mode is present when studying the unaligned (0 mT) ribbon solution only in the perpendicular pump-probe configuration, *i.e.* HV or VH (**Supplementary Note 8**) and not the parallel configurations. In other words – one needs to

probe a dipole perpendicular to the main photoexcitation (that we ascribe to this dark excitonic transition polarised along the PNRs long axis) in order to observe the excited state moving along the B_g^3 vibrational coordinates at the edge of the PNRs.

In summary, we have evidenced *via* SQUID magnetometry and cwEPR, macroscopic magnetism at room temperature in films of PNRs arising from the ribbon edges. In solution a giant magnetic anisotropy means PNRs can be readily aligned with their short axis along the field direction. On photoexcitation, energy rapidly migrates from a bright- to dark-exciton state that is localised to the PNR edge and strongly coupled to a symmetry-forbidden edge phonon mode. Our findings open up extensive opportunities and challenges for further understanding the magnetic properties of PNRs (spin coherence times, influence of ribbon width/strain, role of thickness, *etc*) and for the building of proposed nanoribbon devices^{36,60-63} as well as more disparate applications (non-linear optical elements⁶⁴⁻⁶⁶, nanorobotics^{46,67,68}, magnetic drug delivery⁶⁹). Important questions are raised about the exact microscopic arrangement of spins at the ribbon edge, the in/out-of-plane couplings and couplings between layers. More generally, it remains to further directly link the semiconducting and magnetic properties of PNRs, but the optically active nature of PNR edges provides a promising way for doing so *via* excitation of either the electronic state or edge phonons.

Methods

PNR Synthesis

PNRs were synthesised as reported in Watts *et al.*³⁵. In short, in an argon glovebox (<0.1 ppm O_e, <0.1 ppm H₂O) black phosphorus (2D semiconductors Ltd and Smart Elements) was ground *via* pestle and mortar into ca. 1 mm flakes and 124 mg was transferred to a glass tube fitted with a metal Swagelok valve, alongside 3.5 mg freshly cut lithium metal (Sigma Aldrich, SA, 99% rod). The tube was evacuated (ca. 10⁻⁷ mbar) and cooled to -50 °C and ammonia gas (SA, 99.95%, precleaned by condensation over excess lithium metal) was condensed to submerge the lithium and phosphorus. The solution immediately turned dark blue from the formation of lithium electride, and slowly turned orange over 16 h. The ammonia was then evaporated and the orange LiP₈ salt was dried under vacuum (ca. 10⁻⁷ mbar) at room temperature. The LiP₈ (10 mg) was then placed in 10 mL of either NMP (SA, 99.5% anhydrous) or DMF (SA, 99.9% anhydrous) which had been dried with 4 Å molecular sieves for 1 week. The mixtures were bath sonicated for 30 min, before centrifuging (100g, 10 min) and decanting in a glovebox to give solutions of PNRs.

Atomic Force Microscopy

PNR samples were prepared *via* drop-casting from solution onto freshly cleaved graphite (HOPG) substrates as discussed previously³⁵. High-resolution topography maps were then collected using contact-mode HS-AFM (Bristol Nano Dynamics Ltd, UK) with silicon nitride microcantilevers (MSNL-10, Bruker) with nominal tip radii of 2 nm. To ensure that the images obtained featured tip-limited lateral resolution scan sizes of 0.8 μm × 0.5 μm were used, corresponding to pixel sizes of ~1 nm × 1 nm.

HS-AFM images containing ribbons selected for analysis were input into custom LabVIEW image analysis software (National Instruments) that isolated the ribbon from the background in an automated fashion before generating histograms of ribbon height and width. In brief, the

algorithm consisted of: a local thresholding step to identify the ribbon; a mask step to separate pixels corresponding to the background from the ribbon; an erosion step to remove the edge pixels where the AFM tip traverses the slope between the background and ribbon; calculation of height histograms for both the background and ribbon pixels and finally; Gaussian fits to the histograms recovered the mean height of each and enabled the calculation of the height of the ribbon in respect to the background.

The width of the ribbon was analysed in parallel using the same algorithm. After the masking step the central axis of the isolated ribbon was determined by fitting cubic splines to the two edges of the ribbon and calculating the mean of these two edges. Then, the width of the ribbon was determined by calculating the distance to the central axis from each edge. Measurements of the width of the ribbon along its entire length were then input into a histogram and fit with a Gaussian distribution to identify the mean width of the PNR.

Magnetic Linear Dichroism and Birefringence

The degree of magnetic alignment is measured optically, through the magnetic field-induced linear dichroism (LD) and birefringence (LB), using red and green Helium Neon lasers (wavelengths 632.5 and 543 nm, respectively). The solution samples were contained in an optical cuvette (thickness 5 mm or 10 mm) positioned within a temperature-controlled environment at 20.0 ± 0.1 °C in a 33 T Florida-Bitter electromagnet or a Varian V-3900 2 T magnet. The LD and LB signals were measured using standard polarization modulation techniques using a photo-elastic modulator⁷⁰.

SQUID Magnetometry

Magnetisation measurements were obtained in a Quantum Design Magnetic Properties Measurement System (MPMS 3) using a Superconducting Quantum Interference Device (SQUID) magnetometer. Measurements were performed down to 1.8 K and up to 350 K, in various applied magnetic field strengths up to 7 T. Data for two isothermal magnetic field scans of PNRs out of solution are shown in **Figure 1d**, and two magnetisation-temperature curves of PNRs are displayed in the inset of **Figure 1d**. Each magnetisation-temperature curve was measured starting at 1.8 K and increasing the temperature in a constant probing field of 50 mT. Prior to beginning any new magnetic field or temperature scan the system was taken to 300 K and the magnet was reset to remove any stray flux from the SQUID. Samples were secured on an MPMS quartz sample holder using GE varnish, and care was taken to ensure that they were not touched by any magnetic material throughout the mounting and loading procedure. At each measurement, several dc magnetisation measurements were averaged, providing a reliable measure of the bulk magnetisation of the PNR samples.

While measuring the PNRs in the DMF and NMP solutions (**Supplementary Note 2**) 10 μ L were pipetted into a plastic capsule. The capsule was fixed to a quartz rod using GE varnish, and the presence of the PNR increased the magnetisation by two orders of magnitude when compared to the GE and capsule by itself. The dc moment was averaged over multiple scans, and between each experimental run the MPMS was brought to 300 K and the magnet was reset to remove any remaining flux in the SQUID. Oxygenation of the PNR was performed by introducing by bubbling an O₂ gas stream to the PNR in the plastic capsule while ensuring it does not come into contact with any metallic substances.

Electron Paramagnetic Resonance

For the cwEPR experiments, 100 μL of PNR in DMF solution was filled into a 4 mm outer diameter (3 mm inner diameter) quartz EPR tube, inside a nitrogen glovebox. The sample tube was attached to a custom adaptor and transferred to a pumping station outside the glovebox. The custom adaptor keeps the sample in the inert glovebox environment. The solution was evaporated under vacuum (using a pumping station), resulting in a film on the inner walls of the EPR tube. The procedure was repeated four times, to achieve a thicker film, in total 400 μL was evaporated. The inner wall sample was then left to pump to a pressure of 6×10^{-4} mbar and flame-sealed.

Narrow Magnetic Field Scan - Rotation and Temperature Series (Setup 1):

The cwEPR spectra were recorded at X-band (≈ 9.4 GHz) using a laboratory-built EPR spectrometer (all narrow scan cwEPR spectra were rescaled to 9.4 GHz). The setup consists of a Bruker ER 041 MR microwave bridge together with an ER 048 R microwave controller and an AEG electromagnet together with a Bruker BH 15 Hall effect field controller. The magnetic field was additionally monitored with a Bruker ER 035 M NMR Gaussmeter. The resonator used was a Bruker ER 4122-SHQE resonator. The static magnetic field was modulated at 100 kHz and lock-in detection was carried out using a Stanford Research SR810 lock-in amplifier in combination with a Wangine WPA-120 audio amplifier. An ESR 900 helium flow cryostat together with a ITC503 temperature controller (Oxford Instruments, UK) was used for low temperature measurements. The spectra were acquired at a frequency of ≈ 9.4 GHz with a microwave power of 7.96 mW and 1 mT modulation amplitude. The magnetic field was calibrated using a standard N@C60 sample with a known g -factor.

The narrow magnetic field scans presented in the main text (**Figure 2c**) have had the FMR like signal (slope) removed from them using an appropriate polynomial fit. See **Supplementary Note 4** for further details.

Wide Magnetic Field Scan - Rotation Study (Setup 2):

The cwEPR spectra were recorded at X-band (≈ 9.55 GHz) using a laboratory-built EPR spectrometer (All wide scan cwEPR spectra were rescaled to 9.55 GHz). The setup consists of a Bruker ER 046 XK - T microwave bridge together with an ER 048 R microwave controller and a Varian electromagnet together with a Bruker ER 032M Hall effect field controller. The resonator used was a Bruker MD5 dielectric ring resonator. The static magnetic field was modulated at 99 kHz and lock-in detection was carried out using a Stanford Research SR830 lock-in amplifier in combination with a Wavetek 50 MHz function generator model 80. The wide magnetic field measurement was carried out at 296 K. The spectra were acquired at a frequency of ≈ 9.55 GHz with a microwave power of 7.96 μW and 0.4 mT modulation amplitude.

Transient Absorption Spectroscopy

The transient absorption measurements from 550 – 930nm were performed using a homebuilt setup around a Yb:KGW amplifier laser (1030 nm, 38 kHz, 15 W, Pharos, LightConversion). The probe pulse was a chirped seeded white light continuum created using a 4 mm YAG crystal

that spanned from 500 nm to 950 nm. For the source of the pump pulse (~200 fs) a commercial optical parametric amplifier (OPA) OPHEUS ONE (Light Conversion) was used.

The transient absorption measurements from 400 – 550 nm were performed using a homebuilt setup around a Ti-Sapphire (800 nm, 1 kHz, Spectra-Physics, Solstice Ace). The probe pulse was a chirped seeded white light continuum created using a 4 mm CaF₂ crystal that spanned from 400 nm to 600 nm. For the source of the pump pulse (~100 fs) the fundamental of the laser was doubled in a β -barium borate crystal.

The sub-1T magnetic field was generated using an electromagnet from GMW Model 3470 with 1 cm distance between cylindrical poles and the field strength calibrated with a Gaussmeter.

Impulsive Raman Spectroscopy

A femtosecond time domain Raman spectroscopy measurements were performed using a homebuilt setup around a Yb:KGW amplifier laser (1030 nm, 38 kHz, 15 W, Pharos, LightConversion). The probe pulse was a chirped seeded white light continuum created using a 4 mm YAG crystal that spanned from 500 nm to 950 nm. The pump pulse for the resonant experiment was created using a non-collinear optical parametric amplifier (NOPA) where the 1030 nm seeded a white light continuum stage in sapphire which was subsequently amplified with the third harmonic of the 1030 nm laser in a β -barium borate crystal to create a broad pulse centred at 550 nm. The pump pulse for the off-resonant experiment was created using a non-collinear optical parametric amplifier (NOPA) where the 1030 nm seeded a white light continuum stage in a YAG crystal which was subsequently amplified with the third harmonic of the 1030 nm laser in a β -barium borate crystal to create a broad pulse centred at 750 nm. Both pulses were compressed using a chirped mirror and wedge prism (Layerterc) combination to a temporal duration of under 15 fs. Compression was determined by second-harmonic generation frequency-resolved optical gating (SHG-FROG; upper limit) and further confirmed by reference measurements on acetonitrile where the 2,200 cm⁻¹ mode could be resolved. The probe white light was delayed using a computer-controlled piezoelectric translation stage (Physik Instrumente), and a sequence of probe pulses with and without pump was generated using a chopper wheel (Thorlabs) on the pump beam. The average fluence of the pump 10 μ J /cm².

Temperature dependent Raman spectroscopy and Raman Imaging

Raman spectra were measured as a function of temperature from 4 K to 300 K. Raman measurements were conducted by backscattering (T64000, Horiba) a CW diode line (532 nm, 1 mW). Spectra were collected at > 200 cm⁻¹, where the CCD detector (Horiba Synapse Open-Electrode) has a monotonically increasing quantum efficiency of 0.43 – 0.50. Acquisitions employed a 100 \times optical objective and used minimal laser intensity to avoid sample degradation.

For Raman imaging a standard layout of an epi-detected Raman microscope was used. A pump laser beam (wavelength = 532 nm, Coherent Mira) was spectrally cleaned up by a bandpass filter (FLH05532-4, Thorlabs), and its beam width was expanded to 7.2 mm before entering a home-built inverted microscope. Additional waveplates (half-waveplate and quarter-waveplate for 532 nm, Foctek Photonics) pre-compensated the ellipticity introduced by the dichroic filter (F38-532_T1, AHF) and also generated circularly polarised light. We used high numerical

aperture (NA) oil-immersion objectives (Nikon 60X/1.4 N.A. oil) to ensure high-resolution imaging and increase collection efficiency. Pump power before the objective was 30 mW, a power level that ensured no degradation of samples. The samples were scanned with galvanometric mirrors (Thorlabs). The Raman inelastic backscattered light was collected by the same objective and focused with the microscope tube lens either onto the slit of a spectrometer (Andor, Shamrock 303i, grating 300 l/mm; the slit also acts as an effective pinhole for confocal detection). The spectrometer is equipped with a high-sensitivity charge-coupled camera (Andor, iXon 897). All images presented were taken with integration times/pixel in the 500 ms range. Recording of data was performed by a custom Matlab program. For Raman imaging, black phosphorous flakes (300-600 nm thickness; 2D semiconductors Ltd) were mechanically exfoliated inside a nitrogen glovebox and transferred onto a Si substrate. A 0.15 mm thick coverslip was placed over the flakes and sealed with epoxy glue to act as an encapsulant. The polarisation of the pump and Raman light was not strongly controlled, but simply adjusted to maximise the respective signals.

References

1. Slota, M. *et al.* Magnetic edge states and coherent manipulation of graphene nanoribbons. *Nature* **557**, 691–695 (2018).
2. Wu, X., Zhang, X., Wang, X. & Zeng, Z. Spin density waves predicted in zigzag puckered phosphorene, arsenene and antimonene nanoribbons. *AIP Adv.* **6**, (2016).
3. Rao, S. S. *et al.* Spin dynamics and relaxation in graphene nanoribbons: Electron spin resonance probing. *ACS Nano* **6**, 7615–7623 (2012).
4. Rao, S. S. *et al.* Ferromagnetism in graphene nanoribbons: Split versus oxidative unzipped ribbons. *Nano Lett.* **12**, 1210–1217 (2012).
5. Karakachian, H. *et al.* One-dimensional confinement and width-dependent bandgap formation in epitaxial graphene nanoribbons. *Nat. Commun.* **2020 111** **11**, 1–8 (2020).
6. Rizzo, D. J. *et al.* Inducing metallicity in graphene nanoribbons via zero-mode superlattices. *Science (80-.)*. **369**, (2020).
7. Rizzo, D. J. *et al.* Topological band engineering of graphene nanoribbons. *Nature* **560**, 204–208 (2018).
8. Blackwell, R. E. *et al.* Spin splitting of dopant edge state in magnetic zigzag graphene nanoribbons. *Nature* **600**, 647–652 (2021).
9. Ando, K. Seeking room-temperature ferromagnetic semiconductors. *Science (80-.)*. **312**, 1883–1885 (2006).
10. Burch, K. S., Mandrus, D. & Park, J. Review Waals materials. *Nature* **4–9** (2018)
11. Wilson, N. P. *et al.* Interlayer electronic coupling on demand in a 2D magnetic semiconductor. *Nat. Mater.* **2021 1–6** (2021)
12. Telford, E. J. *et al.* Coupling between magnetic order and charge transport in a two-dimensional magnetic semiconductor. *Nat. Mater.* **21**, 754–760 (2022).
13. Dietl, T. A ten-year perspective on dilute magnetic semiconductors and oxides. *Nat. Mater.* **2010 912** **9**, 965–974 (2010).
14. Ohno, H. *et al.* Electric-field control of ferromagnetism. *Nature* **408**, 944–946 (2000).
15. Koshihara, S. *et al.* Ferromagnetic Order Induced by Photogenerated Carriers in Magnetic III-V Semiconductor Heterostructures of (In, Mn)As/GaSb. *Phys. Rev. Lett.* **78**, 4617–4620 (1997).

16. Náfrádi, B. *et al.* Optically switched magnetism in photovoltaic perovskite CH₃NH₃(Mn:Pb)I₃. *Nat. Commun.* 2016 7 1, 1–8 (2016).
17. Story, T., Gałazka, R. R., Frankel, R. B. & Wolff, P. A. Carrier-concentration-induced ferromagnetism in PbSnMnTe. *Phys. Rev. Lett.* **56**, 777 (1986).
18. Haury, A. *et al.* Observation of a Ferromagnetic Transition Induced by Two-Dimensional Hole Gas in Modulation-Doped CdMnTe Quantum Wells. *Phys. Rev. Lett.* **79**, 511 (1997).
19. Wunderlich, J. *et al.* Coulomb blockade anisotropic magnetoresistance effect in a (Ga,Mn)As single-electron transistor. *Phys. Rev. Lett.* **97**, 077201 (2006).
20. Moreno, M., Trampert, A., Jenichen, B., Däweritz, L. & Ploog, K. H. Correlation of structure and magnetism in GaAs with embedded Mn(Ga)As magnetic nanoclusters. *J. Appl. Phys.* **92**, 4672 (2002).
21. Bae, Y. J. *et al.* Exciton-coupled coherent magnons in a 2D semiconductor. *Nature* **609**, 282–286 (2022).
22. Lee, K. *et al.* Magnetic Order and Symmetry in the 2D Semiconductor CrSBr. *Nano Lett.* **21**, 3511–3517 (2021).
23. Wang, X. *et al.* Spin-induced linear polarization of photoluminescence in antiferromagnetic van der Waals crystals. *Nat. Mater.* **20**, 964–970 (2021).
24. Kang, S. *et al.* Coherent many-body exciton in van der Waals antiferromagnet NiPS₃. *Nature* **583**, 785 (2020).
25. Magda, G. Z. *et al.* Room-temperature magnetic order on zigzag edges of narrow graphene nanoribbons. *Nature* **514**, 608–611 (2014).
26. Zhao, F., Cao, T. & Louie, S. G. Topological Phases in Graphene Nanoribbons Tuned by Electric Fields. *Phys. Rev. Lett.* **127**, 166401 (2021).
27. Gröning, O. *et al.* Engineering of robust topological quantum phases in graphene nanoribbons. *Nat.* 2018 5607717 **560**, 209–213 (2018).
28. Cai, J. *et al.* Atomically precise bottom-up fabrication of graphene nanoribbons. *Nature* **466**, 470–473 (2010).
29. Ruffieux, P. *et al.* On-surface synthesis of graphene nanoribbons with zigzag edge topology. *Nature* **531**, 489–492 (2016).
30. Sisakht, E. T., Fazileh, F., Zare, M. H., Zarenia, M. & Peeters, F. M. Strain-induced topological phase transition in phosphorene and in phosphorene nanoribbons. *Phys. Rev. B* **94**, 085417 (2016).
31. Nourbakhsh, Z. & Asgari, R. Excitons and optical spectra of phosphorene nanoribbons. *Phys. Rev. B* **94**, 1–9 (2016).
32. Wu, Q. *et al.* Electronic and transport properties of phosphorene nanoribbons. *Phys. Rev. B - Condens. Matter Mater. Phys.* **92**, 1–9 (2015).
33. Yang, G., Xu, S., Zhang, W., Ma, T. & Wu, C. Room-temperature magnetism on the zigzag edges of phosphorene nanoribbons. *Phys. Rev. B* **94**, 1–5 (2016).
34. Gibertini, M., Koperski, M., Morpurgo, A. F. & Novoselov, K. S. Magnetic 2D materials and heterostructures. *Nat. Nanotechnol.* 2019 145 **14**, 408–419 (2019).
35. Watts, M. C. *et al.* Production of phosphorene nanoribbons. *Nature* **568**, 216–220 (2019).
36. MacDonald, T. J. *et al.* Phosphorene Nanoribbon-Augmented Optoelectronics for Enhanced Hole Extraction. *J. Am. Chem. Soc.* **143**, 21549–21559 (2021).
37. Vahedi, J. & Peters, R. Edge magnetic properties of black phosphorene nanoribbons. *Phys. Rev. B* **103**, 75108 (2021).
38. Zhu, Z. *et al.* Magnetism of zigzag edge phosphorene nanoribbons. *Appl. Phys. Lett.* **105**, (2014).
39. Poljak, M. & Suligoj, T. Immunity of electronic and transport properties of

- phosphorene nanoribbons to edge defects. *Nano Res.* **9**, 1723–1734 (2016).
40. Golor, M., Wessel, S. & Schmidt, M. J. Quantum nature of edge magnetism in graphene. *Phys. Rev. Lett.* **112**, 1–5 (2014).
 41. Sofer, Z. *et al.* Layered Black Phosphorus: Strongly Anisotropic Magnetic, Electronic, and Electron-Transfer Properties. *Angew. Chemie - Int. Ed.* **55**, 3382–3386 (2016).
 42. Wang, X. *et al.* Highly anisotropic and robust excitons in monolayer black phosphorus. *Nat. Nanotechnol.* **10**, 517–521 (2015).
 43. Van Rhee, P. G. *et al.* Giant magnetic susceptibility of gold nanorods detected by magnetic alignment. *Phys. Rev. Lett.* **111**, 1–5 (2013).
 44. Pietra, F. *et al.* Self-assembled CdSe/CdS nanorod sheets studied in the bulk suspension by magnetic alignment. *ACS Nano* **8**, 10486–10495 (2014).
 45. Shklyarevskiy, I. O. *et al.* Magnetic Alignment of Self-Assembled Anthracene Organogel Fibers. (2005) doi:10.1021/la047166o.
 46. Rikken, R. S. M. *et al.* Manipulation of micro- and nanostructure motion with magnetic fields. *Soft Matter* **10**, 1295–1308 (2014).
 47. Buchner, M., Höfler, K., Henne, B., Ney, V. & Ney, A. Tutorial: Basic principles, limits of detection, and pitfalls of highly sensitive SQUID magnetometry for nanomagnetism and spintronics. *J. Appl. Phys.* **124**, 161101 (2018).
 48. Kuntz, K. L. *et al.* Control of Surface and Edge Oxidation on Phosphorene. *ACS Appl. Mater. Interfaces* **9**, 9126–9135 (2017).
 49. Zhu, X. *et al.* Stabilizing black phosphorus nanosheets via edge-selective bonding of sacrificial C60 molecules. *Nat. Commun.* **2018** *91* **9**, 1–9 (2018).
 50. Ding, B., Chen, W., Tang, Z. & Zhang, J. Tuning Phosphorene Nanoribbon Electronic Structure through Edge Oxidization. *J. Phys. Chem. C* **120**, 2149–2158 (2016).
 51. Peng, X., Copple, A. & Wei, Q. Edge effects on the electronic properties of phosphorene nanoribbons. *J. Appl. Phys.* **116**, (2014).
 52. Hu, W., Lin, L., Zhang, R., Yang, C. & Yang, J. Highly Efficient Photocatalytic Water Splitting over Edge-Modified Phosphorene Nanoribbons. *J. Am. Chem. Soc.* **139**, 15429–15436 (2017).
 53. Nellutla, S., Nori, S. & Singamaneni, S. R. Multi-frequency ferromagnetic resonance investigation of nickel nanocubes encapsulated in diamagnetic magnesium oxide matrix. *J. Appl. Phys* **120**, 223902 (2016).
 54. Zhou, X. *et al.* Effective g factor in black phosphorus thin films. *Phys. Rev. B* **95**, 1–8 (2017).
 55. Mills, D. . Surface anisotropy and surface spin canting in the semi-infinite ferromagnet. *Phys. Rev. B* **39**, 306–307 (1989).
 56. Min, C. K. *et al.* Transient absorption anisotropy study of ultrafast energy transfer in porphyrin monomer, its direct meso-meso coupled dimer and trimer. *J. Chem. Phys.* **114**, 6750–6758 (2001).
 57. Lakowicz, J. R. *Principles of Fluorescence Spectroscopy.* (1983).
 58. Ribeiro, H. B. *et al.* Edge phonons in black phosphorus. *Nat. Commun.* **7**, 1–7 (2016).
 59. Guo, Z. *et al.* From Black Phosphorus to Phosphorene: Basic Solvent Exfoliation, Evolution of Raman Scattering, and Applications to Ultrafast Photonics. *Adv. Funct. Mater.* **25**, 6996–7002 (2015).
 60. Zhao, P., Chauhan, J. & Guo, J. Computational Study of Tunneling Transistor Based on Graphene Nanoribbon. *Nano Lett.* **9**, 684–688 (2009).
 61. Baringhaus, J. *et al.* Exceptional ballistic transport in epitaxial graphene nanoribbons. *Nature* **506**, 349–354 (2014).
 62. Wang, H. *et al.* Graphene nanoribbons for quantum electronics. *Nat. Rev. Phys.* **2021** *312* **3**, 791–802 (2021).

63. Young-Woo Son, M. L. C. & S. G. L. Half-metallic graphene nanoribbons.
64. Carey, B. *et al.* High-Performance Broadband Faraday Rotation Spectroscopy of 2D Materials and Thin Magnetic Films. *Small Methods* 2200885 (2022)
65. Lin, K. Q., Bange, S. & Lupton, J. M. Quantum interference in second-harmonic generation from monolayer WSe₂. *Nat. Phys.* 2019 153 **15**, 242–246 (2019).
66. Chen, Z. Y. & Qin, R. Strong-field nonlinear optical properties of monolayer black phosphorus. *Nanoscale* **11**, 16377–16383 (2019).
67. Zeng, M. *et al.* Autonomous Catalytic Nanomotors Based on 2D Magnetic Nanoplates. *ACS Appl. Nano Mater.* **2**, 1267–1273 (2019).
68. Nguyen, J. *et al.* Magnetic control of graphitic microparticles in aqueous solutions. *Proc. Natl. Acad. Sci. U. S. A.* **116**, 2425–2434 (2019).
69. Shaw, Z. L. *et al.* Antipathogenic properties and applications of low-dimensional materials. *Nat. Commun.* 2021 121 **12**, 1–19 (2021).
70. Kemp, J. C. *Polarized Light and its Interaction with Modulating Devices-a Methodology Review-Polarized Light and Its Interaction With Modulating Devices.* (1987).

Acknowledgements: R.P and A.A thank Russell Cowburn (University of Cambridge) for critical reading of the text and assistance with interpretation of the data, S.S Rao (North Carolina State University) and S.V Bhat (Indian Institute of Science) for discussion of the EPR signals, and Siân Dutton (University of Cambridge) for discussion of the SQUID data.

Funding: A.A. acknowledges funding from the Gates Cambridge Trust as well as support from the Winton Programme for the Physics of Sustainability. S.F. acknowledges funding from the Studienstiftung des deutschen Volkes and the Engineering and Physical Sciences Research Council (EPSRC UK) *via* an EPSRC Doctoral Prize Fellowship. R.P. acknowledges Clare College, Cambridge for funding *via* a Junior Research Fellowship. We acknowledge financial support from the EPSRC *via* grants EP/M006360/1 and EP/W017091/1 and the Winton Program for the Physics of Sustainability. This project has received funding from the European Research Council (ERC) under the European Union’s Horizon 2020 research and innovation programme (grant agreement no. 758826). This work was supported by HFML-RU/NWO-I, member(s) of the European Magnetic Field Laboratory (EMFL) and by EPSRC (UK) *via* its membership to the EMFL (grant no. EP/N01085X/1).

Competing interests: The authors declare that they have no competing interests.

Data and materials availability: The data that support the plots within this paper and other findings of this study are available at the University of Cambridge Repository (<https://doi.org/XXXXXX>).

Author Contributions: A.A. designed and performed optical and magnetic measurements, analysed and interpreted the data and wrote the manuscript. A.J.C, R.R.C.S, T.J.M. and E.S.Y.A. prepared nanoribbon solutions. N.A.P performed and interpreted the EPR experiments under the supervision of J.B.. N.J.M.P and A.E. assisted with SQUID experiments. T.G.P. performed micro-absorption experiments. L.P. performed the high-speed AFM measurements and analysed the results. S.F. and R.C. assisted with optical measurements. M.E.S. and S.K. performed magnetic birefringence and magneto-linear dichroism experiments under the supervision of P.C.M.C who interpreted the results. H.B.A supervised the Raman imaging. C.A.H. supervised the production of nanoribbons, interpreted the data and wrote the manuscript. A.R. and R.H.F. supervised the work of A.A. R.P designed and supervised the project, interpreted data and wrote the manuscript.

Rights Retention Statement: This work was funded the UKRI. For the purpose of open access, the author has applied a Creative Commons Attribution (CC BY) license to any Author Accepted Manuscript version arising.